

Structural and magnetic properties of hexagonal $(\text{Mn,Fe})_{3-5}\text{Ga}$

Boeije, M. F.J.; van Eijck, L.; van Dijk, N.H.; Brück, E.

DOI

[10.1016/j.jmmm.2017.02.058](https://doi.org/10.1016/j.jmmm.2017.02.058)

Publication date

2017

Document Version

Accepted author manuscript

Published in

Journal of Magnetism and Magnetic Materials

Citation (APA)

Boeije, M. F. J., van Eijck, L., van Dijk, N. H., & Brück, E. (2017). Structural and magnetic properties of hexagonal $(\text{Mn,Fe})_{3-5}\text{Ga}$. *Journal of Magnetism and Magnetic Materials*, 433, 297-302.
<https://doi.org/10.1016/j.jmmm.2017.02.058>

Important note

To cite this publication, please use the final published version (if applicable).
Please check the document version above.

Copyright

Other than for strictly personal use, it is not permitted to download, forward or distribute the text or part of it, without the consent of the author(s) and/or copyright holder(s), unless the work is under an open content license such as Creative Commons.

Takedown policy

Please contact us and provide details if you believe this document breaches copyrights.
We will remove access to the work immediately and investigate your claim.

Structural and magnetic properties of hexagonal $(\text{Mn,Fe})_{3-\delta}\text{Ga}$

M. F. J. Boeije,¹ L van Eijck,² N. H. van Dijk,¹ and E. Brück¹

¹*Fundamental Aspects of Materials and Energy, Faculty of Applied Sciences, Delft University of Technology, Mekelweg 15, 2629 JB Delft, The Netherlands*

²*Neutron and Positron Methods in Materials, Faculty of Applied Sciences, Delft University of Technology, Mekelweg 15, 2629 JB Delft, The Netherlands*

(Dated: February 27, 2017)

We have investigated the crystallographic and magnetic properties of $(\text{Mn,Fe})_{3-\delta}\text{Ga}$ alloys. The hexagonal phase is stable between 600 and 700°C and can be stabilized by quenching to room temperature. Mn_3Ga is reported to be off-stoichiometric, but we show that using melt-spinning the stoichiometric compound is attainable. Below the antiferromagnetic transition temperature T_N , the crystal undergoes a hexagonal to monoclinic transition at the distortion temperature T_d . This gives rise to an in-plane rotation of the magnetic moments that is accompanied by a simultaneous increase in magnetization in a magnetic field of 1 T. Fe substitution for Mn removes the monoclinic distortion. Substitutional Fe weakens the antiferromagnetism and a paramagnetic to ferromagnetic transition is observed. The Mn sublattice couples antiparallel throughout the series. Substitution of Ga with Si preserves the monoclinic distortion.

Keywords: magnetoelastic transition; triangular antiferromagnet; antiferromagnetic spintronics

I. INTRODUCTION

Compounds based on Mn and Ga can form a large variety of phases. Properties like a large magnetocrystalline anisotropy, a high spin polarization and high transition temperatures qualify them as good candidates for magnetic materials with high performance like needed for spintronics^{1,2}. On the other hand, moderate Curie temperatures make them interesting for room-temperature applications like magnetic refrigeration. We have studied the magnetic properties of Mg_3Cd -type $(\text{Mn}_{1-x}\text{Fe}_x)_{3-\delta}\text{Ga}$ compounds and found a broad range of transition temperatures.

The Mg_3Cd -type crystal structure is composed of two layers, each containing three magnetic atoms (Mn, Fe or Ni) and one non-magnetic atom (Ga, In, Ge or Sn) in a hexagonal unit cell³. The magnetic atoms are arranged in a triangle in each layer, with a non-magnetic atom above/below the center of this triangle in the other layer, as shown in Fig. 1. This phase is commonly referred to as the ϵ phase. The hexagonal phase is metastable and will form in a temperature range between a high-temperature cubic and a low-temperature tetragonal phase⁴, and can be stabilized by quenching.

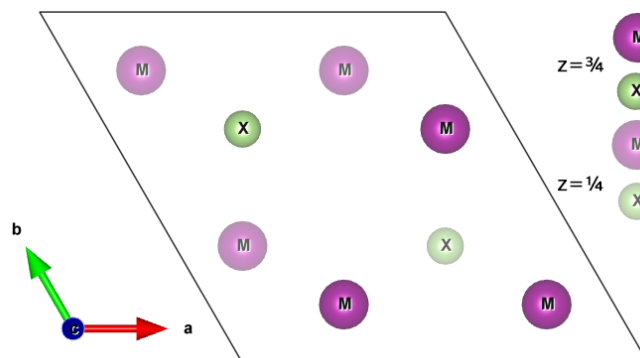


FIG. 1: Unit cell of the Mg_3Cd type crystal structure. Three magnetic atoms (M) are arranged in a triangle in one layer and a non-magnetic atom (X) in the center of the triangle, in the alternate layer indicated by shading.

The first magnetic study on the ϵ phase in the Mn-Ga system showed a magnetic moment of about $3.0 \mu_B$ for Mn⁵. The magnetic moments are arranged in a triangular antiferromagnetic configuration⁶. The triangular arrangement has been described using an Ising model with the spins confined to the basal plane⁷. This gives rise to a complex antiferromagnetic structure that can be described by a combination of three magnetic sublattices, oriented at an angle of 120° . This often leads to exotic properties such as spin ice, multicritical phenomena, and noncollinear ordering⁸.

Most of the triangular spin systems investigated so far are insulators, while Mn_3Ga is an example of a metallic system. This makes this system very interesting. Additionally, there is a sudden change in magnetization that coincides

with a distortion of the lattice at T_d . A hexagonal-to-orthorhombic reduction in symmetry has been reported to take place at the distortion temperature T_d , but no evidence has been presented to confirm this^{1,9}. Using high-resolution X-ray diffraction, we will show that the symmetry is actually reduced to monoclinic. Such a behavior is highly uncommon, $\text{Tb}_3\text{Ag}_4\text{Sn}_4$ is the only other example of such a transition¹⁰.

The outline of the remainder of the paper is as follows, first, the phase stability of the ϵ phase is investigated in the presence of Fe and Si substitutions. To explore if the crystallographic transition persists, the magnetic properties of $(\text{Mn,Fe})_{3-\delta}\text{Ga}$ and $\text{Mn}_{3-\delta}(\text{Ga,Si})$ are reported. Finally, the origin of the crystallographic distortion is investigated using both X-ray and neutron diffraction techniques.

II. EXPERIMENTAL

Mn chips (99,9%), Ga pieces (99,99%) and Fe granules (99,98%) were melted in a custom built arc melting furnace. An extra 2 wt.% Mn was added to account for evaporation losses; the evaporation varied between 1.75 and 2.25 wt.%, based on the change in mass. The obtained buttons were turned three times and subsequently melt spun on a copper wheel spinning at 60 m/s to facilitate the phase formation. Combined evaporation losses from melt spinning and annealing result in a maximum deviation of 0.2 wt.% from the nominal stoichiometry. The melt-spun ribbons were ductile, which is an indication that the ribbons are amorphous.

To find the transition temperatures of the tetragonal, hexagonal and cubic phases, differential thermal analysis (DTA) was performed on a PerkinElmer MAS-5800 instrument with a heating/cooling rate of $10^\circ\text{C}/\text{min}$ and a nitrogen flow rate of 50 ml/min. We observe transitions around 550, 600 and 700°C . These preliminary samples were sealed in quartz ampoules, filled with Ar, and quenched in water. It was found that below 600°C the tetragonal phase is stable and above 700°C the cubic phase is formed. Apart from these phases, no other phases were observed after annealing at 450, 650 and 750°C for 8 h. All subsequent samples were annealed under argon at 650°C for 2 h and quenched in water.

Room temperature X-ray diffraction (XRD) measurements were performed on a PANalytical XPert PRO diffractometer using Co-radiation. The temperature-dependent X-ray diffraction experiments were performed in 0.5 mm capillaries at the BM1A beamline at the ESRF using a wavelength of 0.68884 \AA using a PILATUS2M area detector. Temperature control was achieved using a liquid nitrogen cryostream. Neutron diffraction measurements were performed on the new neutron powder diffractometer PEARL of the TU Delft¹¹. Data were collected at 78 K and 405 K using the (533) reflection of the germanium monochromator ($\lambda = 1.665 \text{ \AA}$). The sample was loaded under argon in a 6 mm diameter air-tight vanadium sample can (0.15 mm thickness). Cooling was achieved using a stream of liquid nitrogen and a heat gun was used for heating. The sample was measured for 10 min. The data treatment consisted of a relative correction for detection efficiency. Rietveld refinement¹² was performed using the FullProf software¹³.

Low-temperature magnetization measurements were performed on a superconducting quantum interference device magnetometer (SQUID; Quantum Design MPMS 5 XL with reciprocating sample option, RSO) while the high-temperature measurements were done on a vibrating sample magnetometer (VSM) with an oven function.

III. RESULTS AND DISCUSSION

A. Phase stability

According to the binary Mn-Ga and Fe-Ga phase diagrams⁴, the ϵ phase is stable only with an excess of Ga. To verify whether this is also the case for melt-spun samples, a stoichiometric Mn_3Ga sample was made. The sample shows single ϵ phase and contains 74.8 ± 0.2 at.% Mn based on the experimental evaporation, EDX measurements show a concentration of 75 ± 2 at.% Mn. All other samples were made with a stoichiometry of 2.9:1 to facilitate the solid solution formation of Mn_3Ga and Fe_3Ga . The results on the phase stability of the samples is summarized in Fig. 2. Above 25% Si substitution, the cubic $\text{Mn}_3(\text{Si,Ga})$ phase is formed. The fraction of the α -Fe phase was found to be strongly dependent on the annealing time. For that reason, the 8 h annealing time of the preliminary samples was reduced to 2 h to reduce the formation of the α -Fe phase. In samples containing Si, between 10% and 25% α -Fe was formed. It is expected that the phase stability window of 600 to 700°C varies with composition. This complicates the phase formation of the ϵ phase and can lead to a non-uniform distribution of second phases.

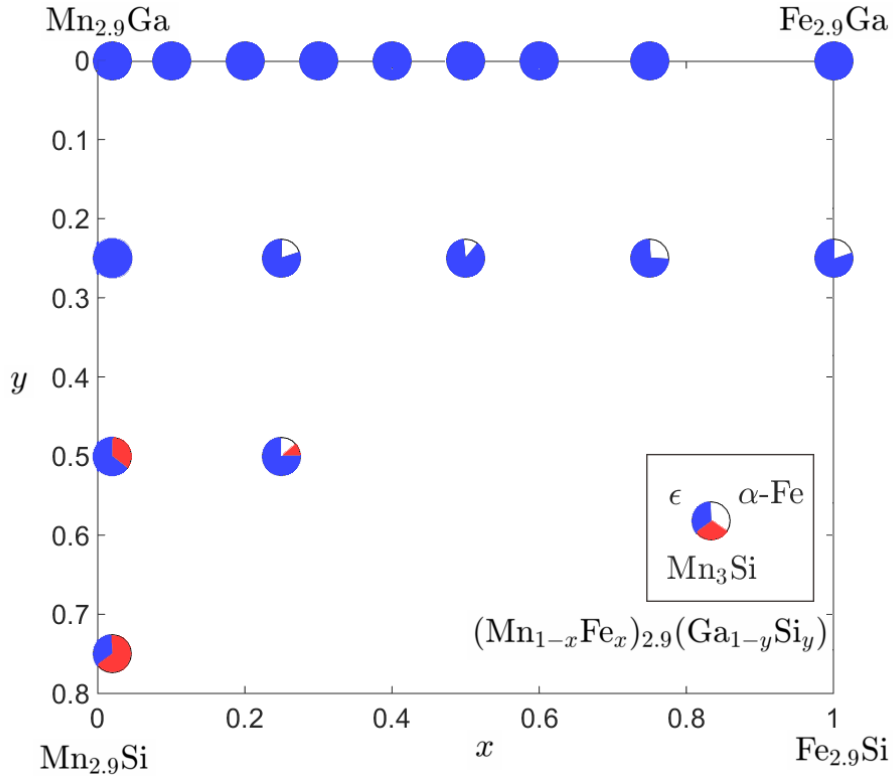


FIG. 2: Quaternary phase diagram of $(\text{Mn,Fe})_{2.9}\text{X}$. The ϵ phase is shown in blue, the cubic Mn_3Si phase is shown in red and the $\alpha\text{-Fe}$ phase is shown in white. All samples were annealed at 650°C for 2h and characterized by XRD at room temperature.

B. $(\text{Mn}_{1-x}\text{Fe}_x)_{2.9}\text{Ga}$

The crystallographic distortion of the hexagonal structure is characterized by an increase in magnetization below room temperature shown in Fig. 3 for $x = 0$. For $x = 0.3$ the antiferromagnetic regime is shifted to lower temperatures and shows two magnetic transitions. For $x = 0.4$ there is a paramagnetic to ferromagnetic transition at 230 K and a ferro- to antiferromagnetic transition at 150 K, where the Mn moments start to align antiferromagnetically. Because the Mn moments cannot compensate each other due to the stoichiometry and the alignment with the applied field, the magnetization increases with decreasing temperature. The same behavior is observed for $x = 0.5$ but is absent for $x = 0.6$.

Fig. 4 shows the magnetization measurements for selected values of x . A very low magnetization is measured for $x = 0.1$, comparable to the magnetization found in Mn_3Ge and Mn_3Sn . In addition, the ferromagnetic component at low fields is absent for $0 < x < 0.3$ and the magnetization increases linearly with applied fields up to 15 T^{14} . The antiferro- to ferromagnetic transition at $x = 0.3$ gives rise to a larger saturation magnetization. To determine the saturation magnetization for all samples, a Langevin function with added linear component was used to fit the data. Above the Néel temperature, the sample shows Curie-Weiss behavior ($\chi = M/H = C/(T + \theta_{CW})$), which is characterized by a linear response of M to the applied field H .

For high Mn concentrations, antiferromagnetic interactions dominate and decrease linearly as a function of x . The same trend is observed for Fe. In the region where T_N and T_C are equal, there is a small deviation from the linear behavior, as shown in Fig. 5. This is in line with the findings on $\text{Mn}_{1-x}\text{Fe}_x)_3\text{Ge}^{15}$ and $\text{Mn}_{1-x}\text{Fe}_x)_3\text{Sn}^{16}$.

Using the experimentally determined saturation magnetization, the magnetic behavior of $(\text{Mn,Fe})_{2.9}\text{Ga}$ is shown in Fig. 6. The line between $x = 0$ and $x = 1$ is shown as a guide to the eye. Three regions can be distinguished: I is characterized by the crystallographic distortion, II is dominated by antiferromagnetic interactions, III is dominated by ferromagnetic interactions. In region II, the magnetization is relatively low. This can be explained by considering a triangular antiferromagnetic arrangement by magnetic moments of unequal magnitude. In region III, the magnetic moments rotate in favor of a ferromagnetic arrangement. The fact that the saturation magnetization does not exceed the value at $x = 1$ indicates that Mn always couples antiferromagnetically, because the magnetic moment of Mn is larger compared to Fe. From the saturation magnetization of $\text{Fe}_{2.9}\text{Ga}$, the calculated magnetic moment per Fe atom is $2.0 \mu_B$. The magnetic properties are summarized in Table I

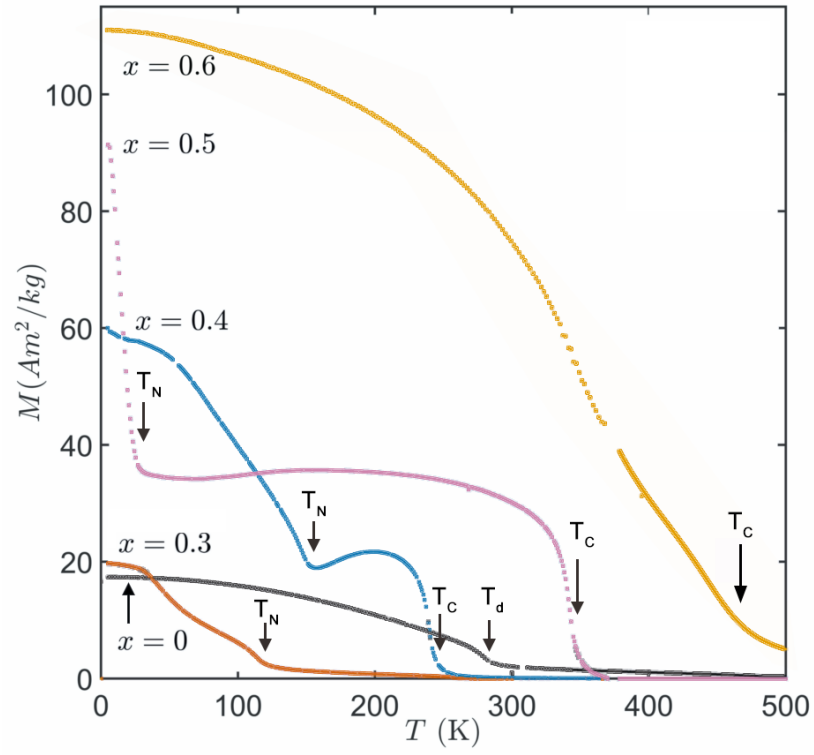


FIG. 3: Magnetization as a function of temperature under an applied field of 1 T for $(\text{Mn,Fe})_{2.9}\text{Ga}$. For $x = 0$, the composition is $\text{Mn}_{2.95}\text{Ga}$.

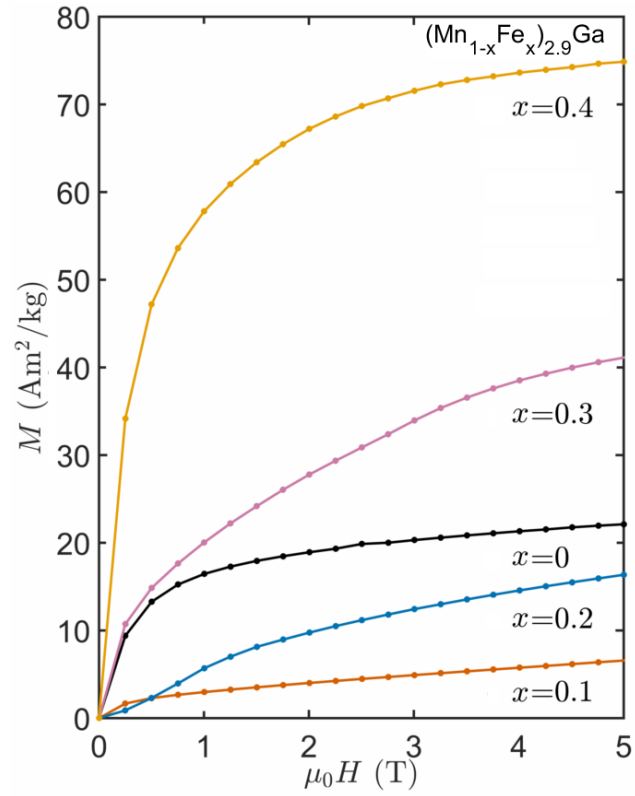


FIG. 4: Magnetization curves and fits as a function of applied field at 5 K.

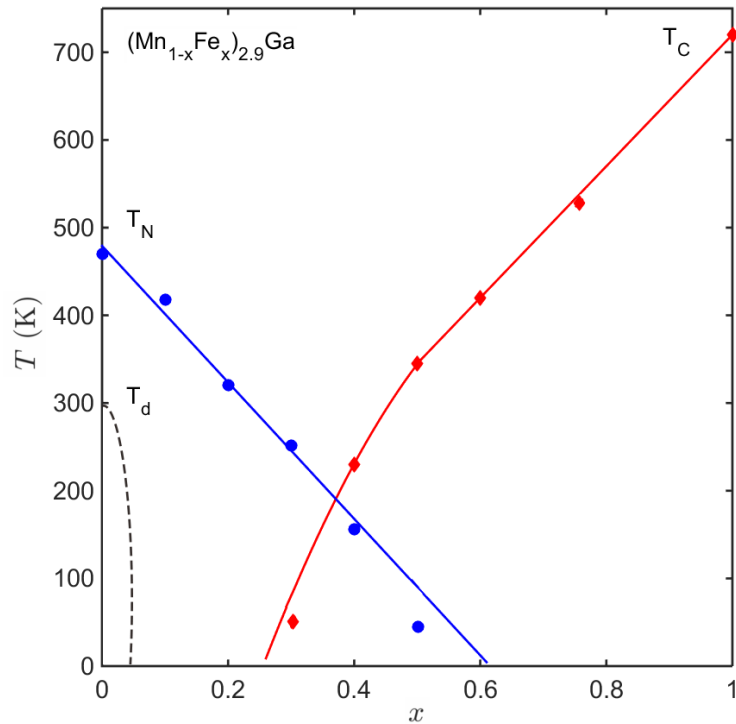


FIG. 5: Critical temperatures of $(\text{Mn}_{1-x}\text{Fe}_x)_{2.9}\text{Ga}$ as a function of x . The antiferromagnetic interaction of $\text{Mn}_{2.9}\text{Ga}$ is weakened for increasing x as the ferromagnetism of $\text{Fe}_{2.9}\text{Ga}$ gradually sets in. The crossover with $T_N \approx T_C \approx 190$ K is around $x=0.37$.

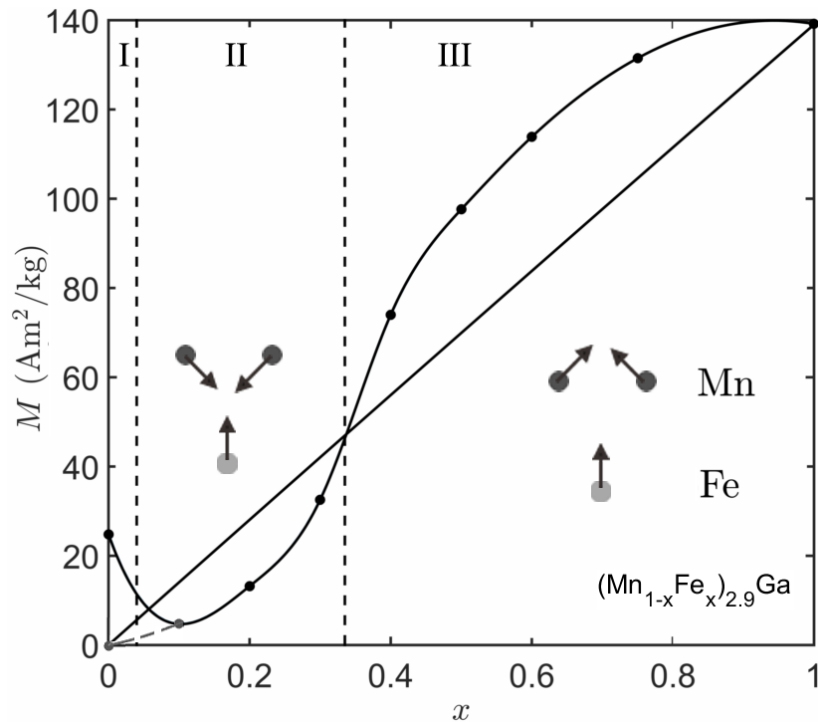


FIG. 6: The experimentally determined saturation magnetization measured as a function of x at 5 K. The datapoints are connected by a cubic spline interpolant as a guide to the eye. In region I, the magnetization is nonzero below T_d and zero above T_d . In region II, below the diagonal line, T_d is absent and the AF Mn sublattice couples AF to the Fe sublattice. In region III, above the diagonal line, the AF Mn sublattice couples FM to the Fe sublattice.

TABLE I: Magnetic transition temperatures T_N and T_C extrapolated to zero-field and saturation magnetization of $(\text{Mn,Fe})_{2.9}\text{Ga}$

compound	T_N (K)	T_C (K)	M (Am^2/kg)	(μ_B / atom)
$\text{Mn}_{2.9}\text{Ga}$	47(0)		20(.0)	0.27
$(\text{Mn}_{0.9}\text{Fe}_{0.1})_{2.9}\text{Ga}$	41(8)		2(.7)	0.04
$(\text{Mn}_{0.8}\text{Fe}_{0.2})_{2.9}\text{Ga}$	32(0)		10(.7)	0.15
$(\text{Mn}_{0.7}\text{Fe}_{0.3})_{2.9}\text{Ga}$	25(1)	5(0)	24(.9)	0.34
$(\text{Mn}_{0.6}\text{Fe}_{0.4})_{2.9}\text{Ga}$	15(6)	23(0)	76(.5)	1.05
$(\text{Mn}_{0.5}\text{Fe}_{0.5})_{2.9}\text{Ga}$	5(0)	34(5)	93(.6)	1.29
$(\text{Mn}_{0.4}\text{Fe}_{0.6})_{2.9}\text{Ga}$		42(0)	111(.8)	1.54
$(\text{Mn}_{0.25}\text{Fe}_{0.75})_{2.9}\text{Ga}$		53(0)	139(.1)	1.91
$\text{Fe}_{2.9}\text{Ga}$		72(0)	145(.7)	2.02

C. $\text{Mn}_{2.95}(\text{Ga,Si})$

When substituting Si for Ga, the crystallographic distortion temperature decreases. To keep the transition temperature around room temperature, a ratio of 2.95:1 was chosen. The unit cell of $\text{Mn}_{2.95}\text{Ga}_{1-y}\text{Si}_y$ reduces isotropically for $y \leq 0.25$ but expands at higher values of y , which suggests that Si first substitutes Ga but for higher Si concentrations it enters the lattice interstitially. At the same time, for $y > 0.25$, the cubic $\text{Mn}_3(\text{Ga,Si})$ phase is formed as a second phase. This second phase is also antiferromagnetic and complicates the analysis of the magnetic properties. The ferromagnetic contribution at low temperatures however persists and the transition broadens. The structural properties are summarized in Table II.

TABLE II: Distortion temperatures, magnetization at 5 K in a field of 1 T (Am^2/kg), lattice parameters a and c and the volume fraction of cubic 2^{nd} phases f_{second} of $(\text{Mn}_{1-x}\text{Fe}_x)_{2.95}(\text{Ga,Si})$.

compound	T_d (K)	a (\AA)	c (\AA)	f_{second} (%)
$\text{Mn}_{2.95}\text{Ga}$	23(0)	5.405(3)	4.350(5)	<1
$\text{Mn}_{2.95}\text{Ga}_{0.75}\text{Si}_{0.25}$	22(0)	5.350(1)	4.313(1)	<1
$\text{Mn}_{2.95}\text{Ga}_{0.5}\text{Si}_{0.5}$	19(0)	5.358(6)	4.320(2)	35
$\text{Mn}_{2.95}\text{Ga}_{0.25}\text{Si}_{0.75}$	15(0)	5.370(8)	4.330(9)	65

D. Crystal distortion

To study the origin of the crystallographic distortion, high-resolution X-ray diffraction measurements were performed as a function of temperature. In order to study a sample that has both a steep increase in magnetization and could be measured well below T_d using liquid nitrogen, the $\text{Mn}_{2.9}\text{Ga}$ sample was selected.

When cooling down the sample, the $\{220\}$ peak gradually splits, indicating a second-order phase transition as shown in Fig. 7. This is supported by DSC measurements that did not detect any latent heat. It seems that the unit cell gradually changes and the resulting symmetry is expected to be a subgroup of the $P6_3/mmc$ spacegroup. The deviation of the 120 degree angle is responsible for the peak splitting, resulting in a hexagonal to monoclinic phase transition. The corresponding space group is $P2_1/m$, which is a subgroup of the orthorhombic space group $Cmcm$, a supercell of the original unit cell¹⁷. The distortion lifts the equivalence of the Mn atoms, they are no longer related by a threefold axis and occupy three crystallographic positions, as summarized in Table III.

By refining the unit cell dimensions, a good fit was obtained with the experimental powder diffraction pattern, shown in Fig. 8. Due to the distortion, both the in-plane angle as well as the cell lengths change, while the out-of-plane cell length is hardly affected. Refinement of the atomic positions of Mn did not improve the fit. The distortion of the triangular lattice of the Mn atoms will affect the magnetic properties. Therefore, neutron diffraction experiments were performed on Mn_3Ga below and above T_d . Above the distortion temperature, the obtained triangular antiferromagnetic arrangement confirms earlier findings⁶. Below the distortion temperature, the degeneracy of the Mn atoms is lifted and the magnetic moments were refined individually. The atomic positions obtained from the XRD refinement were used as input. An increased background was measured at low temperatures around the $\{101\}$ peak, which was attributed to the sample environment. The results are shown in Fig. 9.

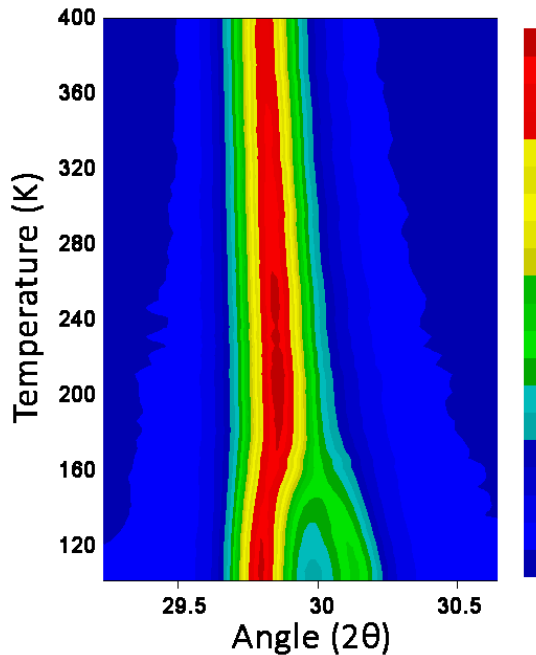


FIG. 7: Powder X-ray diffraction intensity of the $\{220\}$ peak of $\text{Mn}_{2.9}\text{Ga}$ as a function of temperature (K)

TABLE III: Refined X-ray diffraction data of $\text{Mn}_{2.9}\text{Ga}$. The atomic coordinates of Mn1 / Mn2 / Mn3 are split for the monoclinic phase.

	100 K	200 K
S.G.	$P2_1/m$	$P6_3/mmc$
a (Å)	5.304(5)	5.349(7)
b (Å)	4.304(6)	5.349(7)
c (Å)	5.364(3)	4.309(1)
β	119.68(7)	120
Mn	$(x, \frac{1}{4}, z)$ (2e)	$(x, 2x, \frac{1}{4})$ (6h)
x	$\frac{1}{3} / \frac{5}{6} / \frac{5}{6}$	$\frac{1}{6}$
z	$\frac{1}{6} / \frac{1}{6} / \frac{2}{3}$	$\frac{1}{4}$
Ga	$(x, \frac{1}{4}, z)$ (2e)	$(\frac{1}{3}, \frac{2}{3}, \frac{3}{4})$ (2d)
x	$\frac{1}{3}$	$\frac{1}{3}$
z	$\frac{2}{3}$	$\frac{3}{4}$
B_{ov} (Å ²)	0.33	0.61
R_p	4.42	5.85
R_{wp}	3.92	6.51

Above the distortion temperature, the magnetic moments of Mn lie along the crystallographic directions, resulting in a zero net moment. The same holds for the other layer, which has inverse chirality. The chiral solution, where both layers have the same chirality, gives a higher intensity at the $\{100\}$ peak and was discarded. Below the distortion temperature, the net moment cannot point out of plane, as this would be visible in the $\{200\}$ and $\{201\}$ peaks. The rotation of one local moment can reproduce the observed intensity, keeping the magnitude of the moments constant, as shown in Fig. 9. This rotation partially cancels the moment in the $[00\bar{1}]$ direction, leaving a net moment in the $[101]$ direction. The result of the refinements of the neutron diffraction data are summarized in Table IV.

By measuring the magnetization of the sample as a function of temperature, we can see that the magnetization and monoclinic angle are indeed correlated, as can be seen in Fig. 10. The temperature difference can be attributed to the shift due to the applied magnetic field and the temperature control. There is clearly a correlation between the deviation of the 120 degree angle and the rotation of the magnetic moment of the Mn atoms. It is now also clear how the stoichiometry affects the magnetization. In the ferromagnetic state, three magnetic domains are expected to form

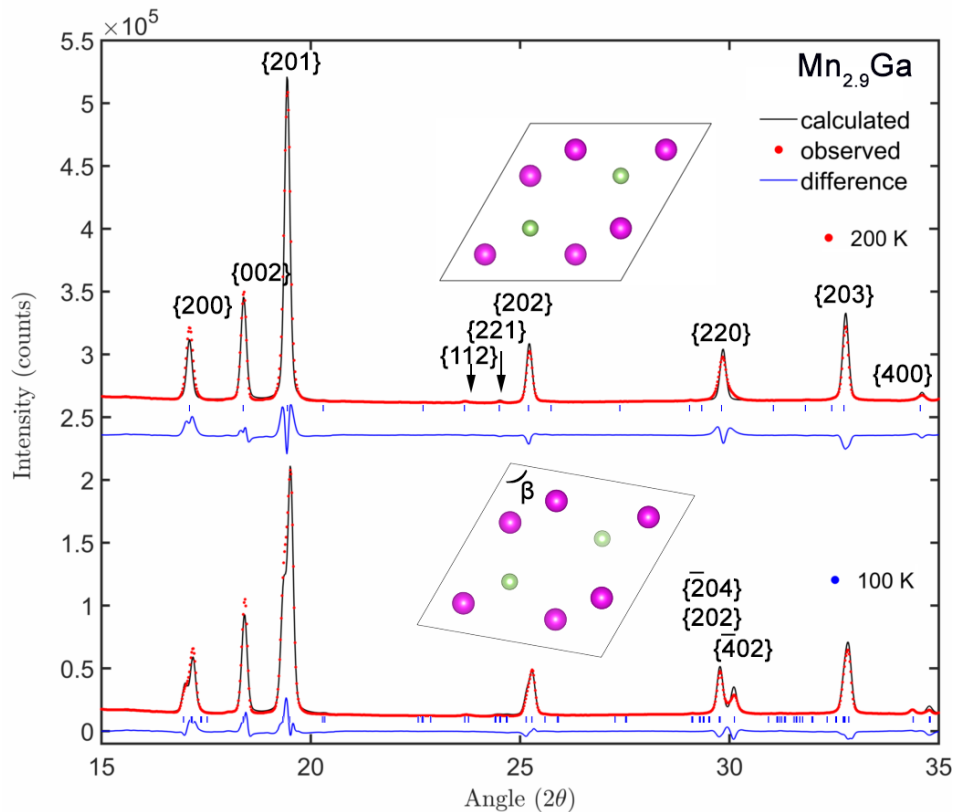


FIG. 8: X-ray diffraction data of $\text{Mn}_{2.9}\text{Ga}$ at a temperature of 200 K (above the distortion temperature) and at 100 K (below the distortion temperature).

TABLE IV: Refined neutron diffraction data of Mn_3Ga . The atomic coordinates obtained by XRD were used as input. The magnetic moment vector is decomposed into three components along the crystallographic axes (M_a, M_b, M_c). The individual moments of Mn are $2.6 \mu_B$ for 78 K and $2.2 \mu_B$ for 405 K.

	78 K	405 K
a (Å)	5.420(9)	5.391(8)
b (Å)	4.333(8)	5.391(8)
c (Å)	5.313(3)	4.348(3)
β	119.18(7)	120
Mn1	(1.6 / 0 / -1.4)	(2.2 / 0 / 0)
Mn2	(0 / 0 / -2.6)	(0 / 2.2 / 0)
Mn3	(-2.6 / 0 / 0)	(-2.2 / -2.2 / 0)
B_{ov} (Å ²)	0.07	1.45
R_p	4.62	4.91
R_{wp}	6.65	6.28

where the in-plane moments generate a net domain magnetization along three principal directions. If one would apply an in-plane magnetic field or shear force on a single crystal, the material would acquire a ferromagnetic component in-plane with a maximum magnetization of about $70 \text{ Am}^2/\text{kg}$. This is a domain reorientation and is expected to be a reversible process. Generally, phase transitions involving a change in symmetry are of first-order. However, in this case, the monoclinic symmetry can be described as a subgroup of the hexagonal symmetry, which allow a continuous change of the 120 degree angle.

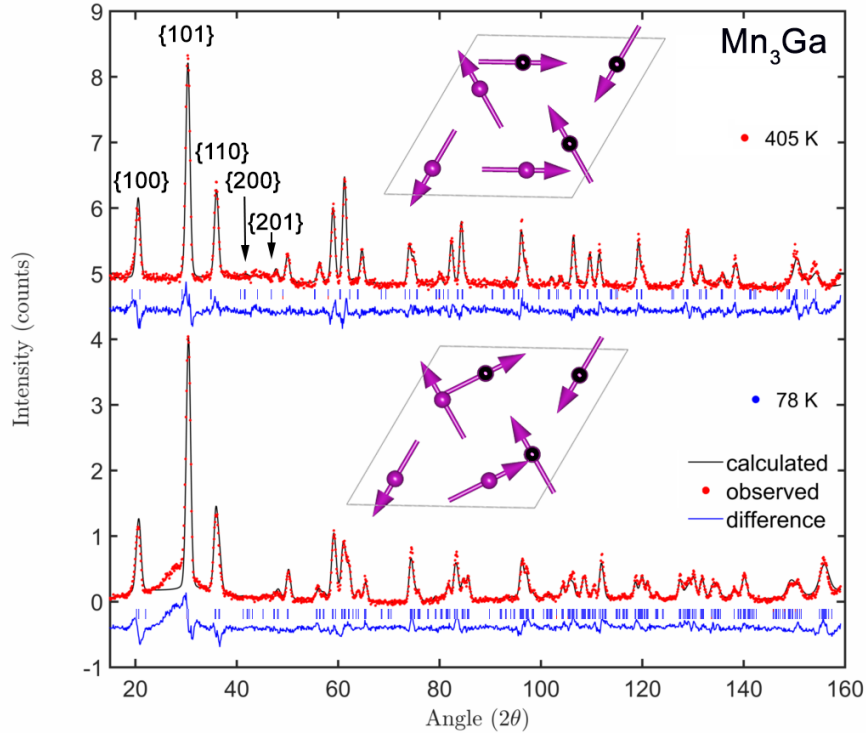


FIG. 9: Neutron diffraction data of Mn_3Ga above and below the distortion temperature. The black and purple atoms lie in different planes. The moment orientations are obtained from Rietveld refinement.

IV. CONCLUSIONS

$(\text{Mn}_{1-x}\text{Fe}_x)_{2.9}\text{Ga}$ is shown to form an ϵ single phase after quenching from a temperature between 600 and 700°. Stoichiometric Mn_3Ga is shown to form using melt spinning, indicating that off-stoichiometry is not an intrinsic property of the material, but is rather an experimental complication. When Si is introduced, the temperature window of phase stability is expected to vary and second and third phases are observed. Magnetization measurements show a low magnetization for Mn rich samples, consistent with an antiferromagnetic arrangement of three magnetic sublattices. When substituting one Fe atom for Mn, a ferromagnetic component is introduced while lowering the Néel temperature. At $x = 0.37$ the Fe and Mn sublattices couple ferromagnetically and the material becomes ferromagnetic. We attribute the crystallographic distortion in $\text{Mn}_{3-\delta}\text{Ga}$ to a rotation of the three antiferromagnetic sublattices below room temperature. This reduces the symmetry from hexagonal to monoclinic via a second-order phase transition. The distortion results in a rotation of one of the magnetic moments in-plane. This effect is linked to the magnetic lattice site, because replacing Ga with Si retains the distortion. This study shows that there is a coupling between the magnetic structure and crystal structure in this material. With the application of a magnetic field, a significant and reversible magnetization change can be realized around room temperature.

V. ACKNOWLEDGEMENTS

The authors thank Bert Zwart for his help in sample preparation, Tjerk Koopmans for high-temperature magnetization measurements, Dmitry Chernyshov for his assistance with high resolution XRD measurements, Kees Goubitz for stimulating discussions, Dimitris Bessas with his assistance with temperature dependent neutron diffraction and Karel Prokeš for his help with Fullprof. This work is part of an Industrial Partnership Program of the Dutch Foundation for Fundamental Research on Matter (FOM) under IPP-i28, co-financed by BASF New Business.

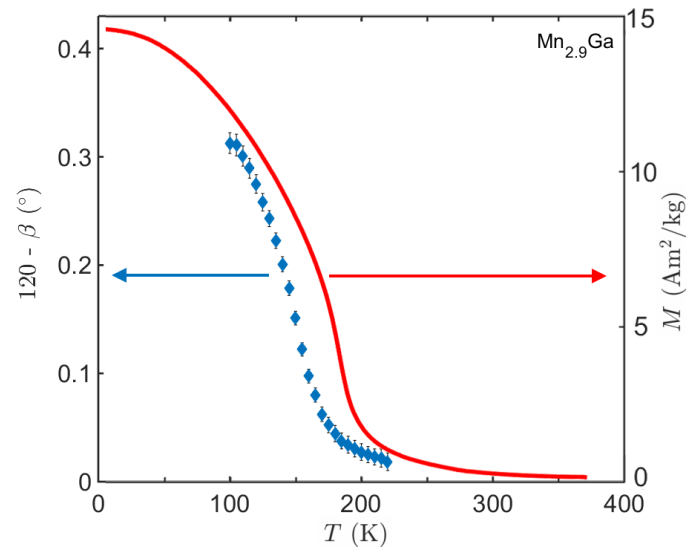


FIG. 10: Distortion of the β angle (left) and magnetization (right) of $\text{Mn}_{2.9}\text{Ga}$ measured at 1 T, as a function of temperature. The magnetization and the distortion are correlated, but don't coincide due to the broadening by the applied field and the temperature control.

References

-
- ¹ H. Kurt, K. Rode, H. Tokuc, P. Stamenov, M. Venkatesan, and J. Coey, *Appl. Phys. Lett.* **101**, 232402 (2012).
 - ² S. Mizukami, F. Wu, A. Sakuma, J. Walowski, D. Watanabe, T. Kubota, X. Zhang, H. Naganuma, M. Oogane, Y. Ando, et al., *Phys. Rev. Lett.* **106**, 117201 (2011).
 - ³ K. Kanematsu and H. Takahashi, *J. Phys. Soc. Jpn.* **53**, 2376 (1984).
 - ⁴ K. Minakuchi, R. Umetsu, I. Kiyohito, and K. Ryosuke, *J. Alloys Compd.* **537**, 332 (2012).
 - ⁵ I. Tsuboya and M. Sugihara, *J. Phys. Soc. Jpn.* **143**, 143 (1963).
 - ⁶ E. Krén and G. Kádár, *Solid State Commun.* **8**, 1653 (1970).
 - ⁷ D. H. Lee, J. D. Joannopoulos, and J. W. Negele, *Phys. Rev. Lett.* **52**, 433 (1984).
 - ⁸ A. P. Ramirez, *Annu. Rev. Mater. Sci.* **24**, 453 (1994).
 - ⁹ H. Niida, T. Hori, and Y. Nakagawa, *J. Phys. Soc. Jpn.* **52**, 1512 (1982).
 - ¹⁰ D. Ryan, J. Cadogan, C. Voyer, M. Napoletano, P. Riani, and L. Cranswick, *Mod. Phys. Lett. B* **24**, 1 (2010).
 - ¹¹ L. van Eijck, L. D. Cussen, G. J. Sykora, E. M. Schooneveld, N. J. Rhodes, A. A. van Well, and C. Pappas, *J. Appl. Crystallogr.* **49**, 1398 (2016).
 - ¹² H. M. Rietveld, *J. of Appl. Crystallogr.* **2**, 65 (1969).
 - ¹³ J. Rodríguez-Carvajal, *Satellite Meeting on Powder Diffraction of the XV IUCr Congress* **127** (1990).
 - ¹⁴ H. Niida, T. Hori, Y. Yamaguchi, and Y. Nakagawa, *J. of Appl. Phys.* **73**, 5692 (1993).
 - ¹⁵ T. Hori, Y. Yamaguchi, and Y. Nagakawa, *J. Magn. Magn. Mater.* pp. 2045–2046 (1992).
 - ¹⁶ T. Hori, H. Niida, Y. Yamaguchi, H. Kato, and Y. Nagakawa, *J. Magn. Magn. Mater.* pp. 159–160 (1990).
 - ¹⁷ M. I. Aroyo, A. Kirov, C. Capillas, J. M. Perez-Mato, and H. Wondratschek, *Acta Cryst.* **A62**, 115 (2006).